Journal of *Marine Science and Engineering*

MDPI

Article

Practical L1-Based Guidance and Neural Path-Following Control for Underactuated Ships with Backlash Hysteresis

Chenfeng Huang [1,*], Bingyan Zhang [1], Haitong Xu [2] and Meirong Wei [3]

[1] Navigation College, Dalian Maritime University, Dalian 116026, China; zby20000522@163.com
[2] Centre for Marine Technology and Ocean Engineering (CENTEC), Universidade de Lisboa, 1049-001 Lisbon, Portugal; haitong.xu@centec.tecnico.ulisboa.pt
[3] Navigation College, Jimei University, Xiamen 361021, China; weimr@jmu.edu.cn
* Correspondence: chenfengh@dlmu.edu.cn

Abstract

The study addresses trajectory tracking control for underactuated vessels with uncertain backlash-type hysteresis. First, an improved practical L1-based guidance strategy is developed by embedding the L1 mechanism into the virtual ship framework to eliminate steering overshoot and yaw angle error accumulation, which can facilitate the smooth turning of ships along waypoint-based paths with large curvature. Next, to mitigate control performance degradation induced by backlash-like hysteresis nonlinearity, an improved quadratic function is utilized to boost the closed-loop system's convergence capability. Moreover, system model uncertainty-induced perturbations are compensated using the resilient neural damping method, which can simplify the structure and reduce the computation burden of the proposed controller. Utilizing Lyapunov-based approaches and the special Young's inequality, uniformly ultimately bounded stability over a semi-global domain is established. Finally, numerical simulations are executed to validate the efficacy of the developed control architecture.

Keywords: backlash hysteresis; underactuated vessel; L1-based guidance; integer power; path-following control

1. Introduction

Over the past few years, many studies have been conducted on nonlinear systems, and a series of successes have been achieved. Underactuated marine vehicles refer to non-fully actuated nonlinear dynamical systems with control deficiency, with respect to system DOFs, which usually arises from non-holonomic systems with unsolvable constraints [1–7], and such systems are superior to fully-driven systems in terms of energy saving, cost reduction and system efficiency [8,9]. Among them, marine ships are typical representatives of mechanical systems with actuator deficiency [10], while trajectory tracking and stabilization for thrust-deficient marine vessels have attracted accelerated focus in the current technological cycle as a persistent feedback synthesis problem. The dynamical model of underactuated marine vessels violates Brockett's necessary conditions [11], the error dynamics defy stabilization via classical continuous time-invariant feedback [12]. Consequently, diverse discontinuous and time-variant control strategies have been developed to address underactuation in marine vessels, including, but not limited to, variable structure control, nonlinear control and robust synthesis methods.

To facilitate the ship path following tasks for different routes, a guidance mechanism is usually employed to synthesize dynamic yaw reference signals for autonomous vessels.

Check for updates

Academic Editor: Rafael Morales

Received: 19 December 2025
Revised: 13 February 2026
Accepted: 19 February 2026
Published: 22 February 2026

Copyright: © 2026 by the authors. Licensee MDPI, Basel, Switzerland. This article is an open access article distributed under the terms and conditions of the Creative Commons Attribution (CC BY) license.

Among various guidance strategies, the direct visual guidance vector (DVG) technique is widely adopted because of its simplicity and effectiveness. The DVG-based projection algorithm is firstly designed for underactuated ships in [13], which the minimization of cross-track errors to a predefined path is achieved and the command of the heading angle is computed for the ship's autopilot system. In [14], a new DVG guidance algorithm is developed to transform the heading error by formulating the waypoints reference path as variable acceptable radius, and the model predictive control (MPC) scheme is presented to design robust trajectory tracking controllers for thrust-constrained vessels under model perturbations. To achieve a specified DVG interception angle between the unmanned surface vehicles (USVs) and moving targets, an innovative terminal DVG guidance strategy is proposed for USVs in [15]. Though a diversity of DVG-based guidance algorithms have been applied in marine tasks, the accurate guidance for large curvature reference paths remain unresolved. To facilitate the smooth turning for waypoint-based path, a real-time virtual ship emulator with dynamic virtual ship (DVS) is originally engineered for underactuated ships in [16]; a comparison simulation is benchmarked against the conventional DVG algorithm, and extensive simulations quantitatively demonstrate the proposed method's enhanced performance in tracking accuracy and computational efficiency. Considering the collision avoidance of multiple static and moving obstacles, an enhanced DVS framework is introduced in [17] to compute live attitude command signals for underactuated marine vessels, where COLREGs adherence is guaranteed by dynamic exclusion zone configuration.

As a typical input nonlinearity, hysteresis exists widely in a variety of mechanical systems [18–26], which seriously limits the performance of controllers and may even lead to failure and divergence of the feedback-regulated systems. In recent years, the nonlinear control of mechanical systems considering hysteresis characteristics [27] has gradually become a hot spot for researchers. Various hysteresis models have been proposed; representative hysteresis modeling approaches include the backlash-like hysteresis model [28], the Bouc–Wen differential model [29] and the Duhem model [30]. Among them, backlash-like hysteresis is more adopted because of its accurate description of hysteresis nonlinearity. For the maneuvering and control of underactuated ships, the rudders and propellers also suffer from performance degradation due to actuator hysteresis. Compared to amplitude saturation, dead-zone nonlinearity, and other actuator nonlinearity, backlash-like hysteresis is often neglected in controller design of underactuated ships, resulting in problems of low accuracy, slow response and signal oscillation. To address the aforementioned problems, a novel asynchronous event-triggered control architecture is presented for ship dynamic positioning systems in [31]; the backlash-like hysteresis is utilized to emulate the nonlinearity of the thruster. Considering the hysteresis effect on the ship's motions, a novel memory feedback shake-reducing strategy is presented to control the pitch-roll motion under stochastic disturbance [32]. To eliminate the hysteresis effect induced by the dynamic stall of ship fins, a constrained model predictive control strategy is proposed in [33] by estimating the effective attack angle. In [26], a nonlinear adaptive fuzzy robust control scheme with disturbance rejection capability was developed for a micro-positioning actuator to eliminate hysteresis effects and modeling uncertainties. However, path following and attitude stabilization for underactuated vessels remain persistent core challenges in maritime control systems. Existing mainstream vessel guidance methods, such as DVG, fail to address precise guidance along high-curvature reference paths. These approaches suffer from steering overshoot and cumulative yaw angle errors, making it difficult to achieve smooth vessel turns along high-curvature waypoint-based paths. With the advancement of autonomous shipping technology, the demand for smooth path following control along waypoint paths—particularly those with high curvature—has become increasingly urgent.

In this paper, a practical L1-norm guidance with a robust neural control strategy is designed for non-fully actuated ship dynamics subject to backlash hysteresis. The key innovations of this study are summarized below:

(1) To facilitate the ship path following guidance for large curvature reference paths, an improved L1 norm-based guidance principle is designed upon the DVS framework. By predicting the position deviation of the vessel at a future time point, yaw acceleration commands are generated to optimize the ship heading and speed. Consequently, tracking accuracy and stability on high-curvature paths are significantly enhanced, while oscillations are reduced.

(2) Accounting for the performance deterioration induced by the backlash hysteresis of actuators, the quadratic function is employed to enhance the closed-loop robustness, and a low-frequency path-following controller is developed with the neural damping technique. Compared with conventional strategy [14], the proposed controller features a simplified structure and reduced computational complexity. By optimizing filtering algorithms, it reduces real-time computational load while maintaining accuracy, thereby enhancing suitability for practical engineering applications.

This manuscript is structured in the following manner: Section 2 introduces the mathematical model and problem formulation. Section 3 includes the comprehensive architecture of the L1 norm-based guidance principle. Section 4 details the systematic framework for the controller design, with stability analysis and performance assessment formulated through exact computational Lyapunov approaches. Section 5 presents numerical simulation outcomes verifying the controller's performance. Section 6 presents the final conclusion.

2. Problem Statement and Preliminary Background

In this paper, $|\cdot|$ is used to denote the absolute value function applied to a scalar quantity. $\|\cdot\|$ stands for the ℓ_2-norm (standard Euclidean norm) in vector space. $\lambda_{\min}(\cdot)$ stands for the matrix's smallest eigenvalue. The notation $\tilde{(\cdot)} = (\cdot) - \hat{(\cdot)}$ is used, $\hat{(\cdot)}$ being the maximum likelihood estimate of $(\cdot)$.

2.1. Underactuated Ship Dynamics with Backlash Hysteresis

According to Newton-Euler and Lagrangian formulations of classical mechanics [13], the horizontal-plane dynamics of an underactuated marine vessel is governed by the following 3-DoF equations:

$$\begin{bmatrix} \dot{x} \\ \dot{y} \\ \dot{\psi} \end{bmatrix} = \begin{bmatrix} \cos\psi & -\sin\psi & 0 \\ \sin\psi & \cos\psi & 0 \\ 0 & 0 & 1 \end{bmatrix} \begin{bmatrix} u \\ v \\ r \end{bmatrix} \tag{1}$$

$$\begin{bmatrix} m_u\dot{u} \\ m_v\dot{v} \\ m_r\dot{r} \end{bmatrix} = \begin{bmatrix} m_v r v \\ -m_u r u \\ (m_u - m_v)uv \end{bmatrix} + \begin{bmatrix} -f_u \\ -f_v \\ -f_r \end{bmatrix} + \begin{bmatrix} \tau_u \\ 0 \\ \tau_r \end{bmatrix} + \begin{bmatrix} d_{wu} \\ d_{wv} \\ d_{wr} \end{bmatrix} \tag{2}$$

where $\eta = [x,\ y,\ \psi]^\top$ defines the vessel's pose in the inertial reference frame, while $v = [u,\ v,\ r]^\top$ represents velocity components in the body-attached frame. The control inputs τ_u and τ_r actuate the vessel's surge and yaw dynamics, respectively. m_u, m_v, m_r are ship added mass parameters in surge, sway and yaw directions, and the disturbances d_{wu}, d_{wv} and d_{wr} encapsulate the aggregated effects of waves, wind, and currents. High-order hydrodynamic interactions are modeled via the state-dependent nonlinearities f_u, f_v, and f_r, mapping velocity v to force/moment perturbations.

Considering the ship servo system comprises the backlash-type hysteretic nonlinearity [34] as described by (3):

$$\frac{d\delta_i}{dt} = \Lambda \left| \frac{d\delta_i^\circ}{dt} \right| (c\delta_i^\circ - \delta_i) + B_1 \frac{d\delta_i^\circ}{dt}, i = u, r \tag{3}$$

where $\delta_i = \tau_i$, the parameter c quantifies the gradient of the backlash hysteresis operator's transition region, Λ, B_1 are model parameters, satisfying $c > B_1$, $c > 0$. By referring to [35], the following equation can be derived.

$$\delta_i(t) = c\delta_i^\circ(t) + d(\delta_i^\circ) \tag{4}$$

with

$$\begin{aligned} d(\delta_i^\circ) = {} & (\delta_{i0} - c\delta_{i0}^\circ) e^{-\Lambda(\delta_i^\circ - \delta_{i0}^\circ)\mathrm{sgn}(\dot{\delta}_i^\circ)} \\ & + e^{-\Lambda\delta_i^\circ \mathrm{sgn}(\dot{\delta}_i^\circ)} \int_{\delta_{i0}^\circ}^{\delta_i^\circ} (B_1 - c) e^{\Lambda\eta \mathrm{sgn}(\dot{\delta}_i^\circ)} \, d\eta \end{aligned} \tag{5}$$

where δ_{i0} and δ_{i0}° serve as initial values for δ_i and δ_i°. $d(\delta_i^\circ)$ is bounded and satisfies $d(\delta_i^\circ) < \bar{d}(\delta_i^\circ)$, where $\bar{d}(\delta_i^\circ)$ denotes an unknown parameter [28]. The nonlinearity of hysteresis with backlash characteristics is shown in Figure 1; the system parameters are configured as $\Lambda = 1$, $B_1 = 0.346$, with the time-varying reference signal set as $\delta_i^\circ(t) = 3.5\sin(2.3t)$. The initial state vectors satisfy $\delta_i^\circ(0) = \delta_{i0}(0) = 0$.

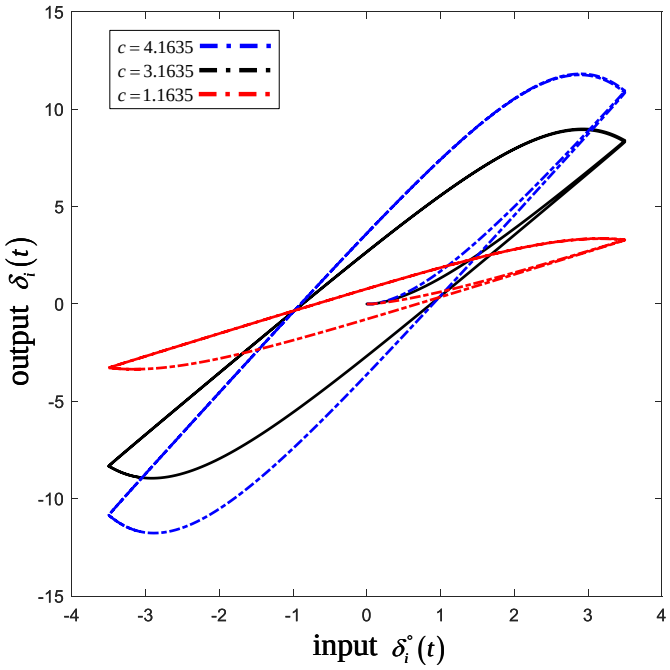


Figure 1. Hysteresis curves with different parameter c.

Figure 1 is produced based on the hysteretic nonlinear model described in (3) and (4) of the reference text. This diagram visually illustrates the hysteretic nonlinear characteristics of the mechanical servo system, presenting the non-one-to-one mapping relationship between the input and output of the hysteretic model under different gradient parameters c. Each curve corresponds to a set of c values, all exhibiting a typical hysteretic loop shape, reflecting the non-one-to-one input-output mapping characteristic of backlash-type nonlinearity.

Combining the surge and yaw dynamics (4) with the main system model (2) yields

$$\begin{aligned} \dot{u} &= \frac{m_v}{m_u} vr - f_u + \frac{1}{m_u}(c\delta_u^{\circ}(t) + d(\delta_u^{\circ})) + d_{wu} \\ \dot{r} &= \frac{(m_u - m_v)}{m_r} uv - f_r + \frac{1}{m_r}(c\delta_r^{\circ}(t) + d(\delta_r^{\circ})) + d_{wr}. \end{aligned} \tag{6}$$

2.2. Neural Network-Based Function Approximation

Leveraging its universal approximation capability, the Gaussian kernel-based neural architecture serves as a powerful tool for nonlinear function modeling, as demonstrated in [36]. In this section, we will use RBF-NNs to handle the unknown uncertainty of ship dynamics so as to facilitate the controller design for the path-following task.

Lemma 1. *For an arbitrary continuous function $h(\boldsymbol{\chi})$ satisfying $h(\mathbf{0}) = 0$ with compact support in $\Omega_\chi \in \mathbb{R}^m$, the function $h(\boldsymbol{\chi})$ can be universally approximated via Gaussian kernel networks with decoupled continuous operators.*

$$g(\boldsymbol{\chi}) = O^\top R(\boldsymbol{\chi}) + e(\boldsymbol{\chi}) \ , \ \forall \boldsymbol{\chi} \in \Omega_\chi \tag{7}$$

the ideal weight vector $O = [o_1, o_2, \ldots, o_l]^\top$ is constant, and the approximation error $e(\boldsymbol{\chi})$ satisfies supremum norm $|e(\boldsymbol{\chi})| \leq \bar{e}$, with $\bar{e}$ a priori unknown. $R(\boldsymbol{\chi}) = [r_1(\chi), r_2(\chi), r_l(\chi)]^\top$ is an RBF vector selected as a Gaussian function.

$$r_j(\chi) = \frac{1}{\sqrt{2\pi}\eta_j} \exp\left[-\frac{(\chi - \mu_j)^\top (\chi - \mu_j)}{2\kappa_j^2} \right], j = 1, 2, 3, \ldots, l \tag{8}$$

where μ_j is the receptive field center, κ_j stands for the Gaussian function's width parameter, l stands for the total number of neurons in the network, j indicates the state vector's dimension χ.

Lemma 2. *Given $\forall (m, n) \in \mathbb{R}^2$, the following inequality is satisfied:*

$$mn \leq \frac{\gamma^r}{r}|m|^r + \frac{1}{s\varepsilon^s}|n|^s \tag{9}$$

where $\gamma > 0, s > 1, r > 1$, and $(s-1)(r-1) = 1$.

Lemma 3. *Suppose we need to work with cubic terms of the form m^3, and we aim to derive an inequality that bounds m^3 using higher-order polynomial terms:*

$$m^3 \leq a^4 + b^4. \tag{10}$$

Utilizing Young's inequality allows us to obtain this relationship. According to Young's inequality, given a form of a positive number, for example, set the choices $r = 3$ and $s = 4/3$.

$$m^3 = mnm \leq \frac{m^4}{4/3} + \frac{n^4}{4} \tag{11}$$

To do this, we can choose n so as to relate it to some appropriate m, n. Usually, by fixing $n = k_1 m$ (some constant), we can obtain a new inequality. The final approximate form may be:

$$m^3 \leq \frac{m^4}{4} + \frac{k_1^4 m^4}{4} \tag{12}$$

after setting k_1 appropriately, the desired form can be found.

The fact that the cubic form can eventually be expressed as a relationship between two quadratic forms is meant to take advantage of the flexibility of the inequality, and the common result is:

$$m^3 \leq \frac{m^4}{4} + \frac{m^4}{4}$$

The exact choice and the value of the constants to be judged will vary according to the actual situation.

3. L1 Dynamic Guidance Rate

In this paper, for the ship tracking guidance problem based on the waypoint-generated path, an improved guidance strategy based on a virtual ship model is proposed. That is to say, through the constant change of the DVS distance from the direct distance of the preset path to provide reference signals for the physical vessel, to achieve waypoint-proximate maneuver continuity with minimal-path adjustment.

Consider that the desired path is produced by a simulated vessel model as follows:

$$\begin{aligned} \dot{x}_d &= u_d \cos(\psi_d) \\ \dot{y}_d &= u_d \sin(\psi_d) \\ \dot{\psi}_d &= r_d \end{aligned} \tag{13}$$

where variables carry the same meanings as in (1), and the desired paths x_d, y_d and ψ_d are uniformly bounded with their first derivatives.

In practical scenarios, the reference path is constructed by interpolating waypoints $W_i = (x_i, y_i)$ through piecewise linear segments and smooth arcs (Figure 2). In the context of straight segments, the path-following task employs the DVS steering law to determine the required course angle, thus enabling the fulfillment of control goals. the simulated vessel travels in the straight line section with a fixed surge velocity u_d, which is a positive user-defined constant, while r_d represents an order that changes over time. Along the straight-line paths, $r_d = 0$. Along the smooth curved arcs, it is changing. First, the angle of the segment $W_{i-1}W_i$ is calculable from

$$\phi_{i-1 \to i} = \arctan \frac{y_i - y_{i-1}}{x_i - x_{i-1}} \tag{14}$$

Then, we define $\Delta\phi_i$ as the difference between consecutive bearing angles $\phi_{(i \to i+1)}$ and $\phi_{(i-1 \to i)}$.

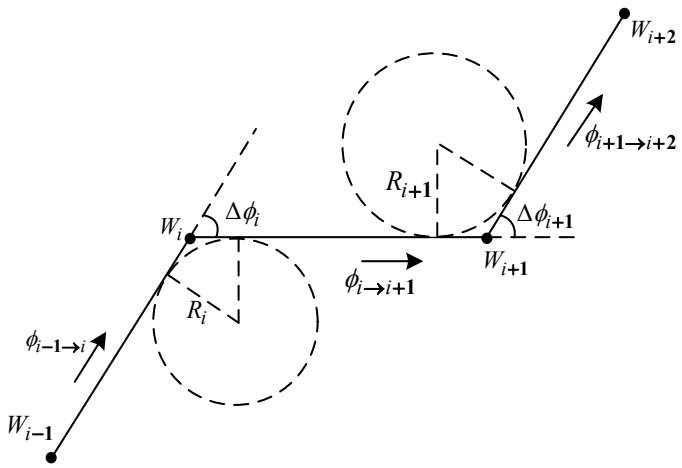


Figure 2. The diagram of waypoint-based path.

The changing L1 guidance rate is calculated by calculating the sway deviation of the current position from the desired path and combining it with the l_1 to generate the desired sway acceleration command to adjust the direction of motion to make the vessel come out of the smooth curve. Since underactuated vessels do not have a sway actuator, it is not possible to generate the sway force directly, but it is possible to indirectly control the sway displacement by adjusting the heading angle and utilizing the sway component of the forward speed. For example, the change in heading angle will deflect the ship's direction of motion, thus generating an equivalent sway acceleration. The sway acceleration generated by l_1 can be converted into a heading angle rate command r_d, which in turn is realized by rudder angle control, and at the same time the command is generated by controller tracking. By providing a reference signal through the position change of the DVS on the ship's target path and feeding the position information from the DVS to the USV, we can perform ship guidance through the constant change of the distance l_1 (Figure 3).

$$a_{cmd} = \frac{2u_d^2}{l_1} \sin \eta \tag{15}$$

where a_{cmd} denotes sway acceleration perpendicular to the direction of velocity. l_1 represents the virtual distance, that is, the vertical distance from the current position of the simulated vessel to the target path. l_1 is dynamically adjusted and proportional to the speed of the simulated ship.

$$l_1 = ku_d \tag{16}$$

where k is the scale factor.

At the same time, l_1 is related to the vertical distance from the unmanned ship to the target path.

$$l_1 = \sqrt{d^2 + e} \tag{17}$$

where d is the vertical distance and e is a constant to avoid l_1 being too small. At the turning point, the acceleration command calculated through the above equation is made equal to the centripetal acceleration tracking this instantaneous arc, which in turn gives the DVS the correct reference signal to provide to the real ship, and the r_d derived through $r_d = a_{cmd}/u_d$ can be used to control the steering of the DVS, and a similar process is repeated for each waypoint to finalize the route generation. The residual computational error is dynamically recomputed using l_1 updated data streams, preventing error propagation through iterative refinement.

Assumption 1. *There exist practical bounds* $|d_{wu}| \leq d_u^{\mathrm{ub}}$, $|d_{wv}| \leq d_v^{\mathrm{ub}}$, $|d_{wr}| \leq d_r^{\mathrm{ub}}$, *where superscript* 'ub' *denotes unknown upper bounds.*

Assumption 2. *It is assumed that the sway velocity exhibits passive boundedness, following [37].*

Remark 1. *In Assumption 2, when a vessel navigates in actual marine environments, all environmental disturbances are constrained by physical laws and cannot exhibit infinitely large perturbations. Such environmental disturbances directly manifest as additional perturbations in the vessel's surge velocity, sway velocity, and yaw velocity. Consequently, the corresponding disturbances must possess objective physical boundaries.*

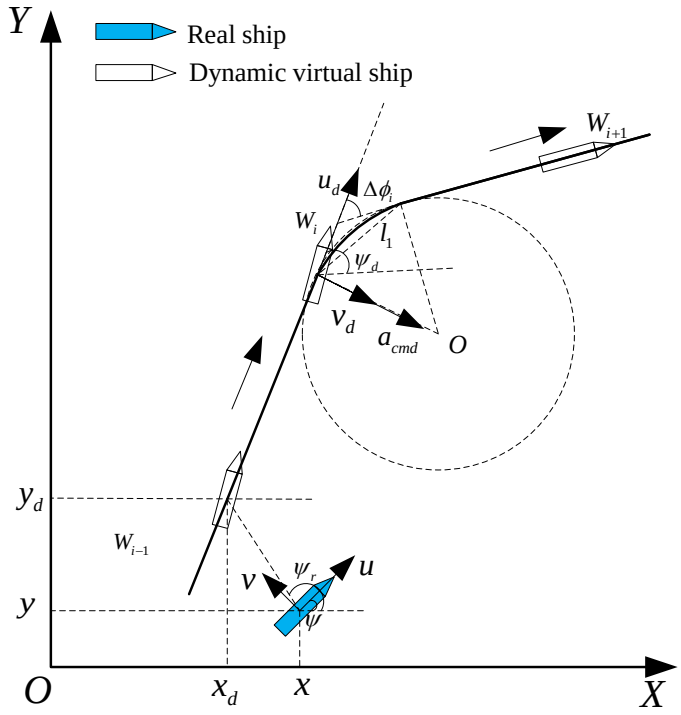


Figure 3. L1 Dynamic Guidance Rate.

4. Neural Damping-Based Path-Following Controller Design

Leveraging the DSC and MLP methodologies presented in [38,39], we design an neural damping path following controller of underactuated vessels. Figure 4 depicts the structure of ship control framework.

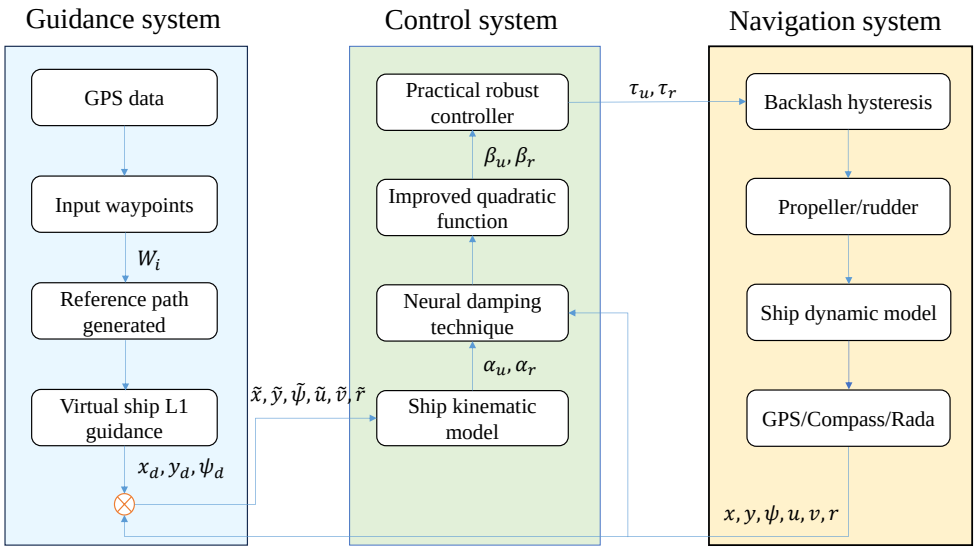


Figure 4. The diagram of the controller design.

4.1. Controller Design

Within this part, the dynamic surface control method is integrated into the design workflow. The virtual control function is given to stabilize by choosing the appropriate Lyapunov function, and finally the actual controller is designed.

Step 1: The tracking error dynamics admit the formal representation:

$$\begin{aligned} \tilde{x} &= x_d - x \\ \tilde{y} &= y_d - y \\ \tilde{z} &= \sqrt{\tilde{x}^2 + \tilde{y}^2} \\ \tilde{\psi} &= \psi_R - \psi \end{aligned} \tag{18}$$

where the relative bearing angle ψ_R is confined to the interval $(-\pi, \pi]$, representing the orientation from the vessel's current position to the target waypoint, and distinct from the yaw angle ψ_d of the simulated vessel.

$$\psi_R = \frac{\pi}{2}\{1 - sgn(\tilde{x})\}sgn(\tilde{y}) + \arctan\left(\frac{\tilde{y}}{\tilde{x}}\right). \tag{19}$$

It is easy to get the following:

$$\begin{aligned} \tilde{x} &= \tilde{z}\cos(\psi_R) \\ \tilde{y} &= \tilde{z}\sin(\psi_R). \end{aligned} \tag{20}$$

Combining (6), (18), and (20), error variables $\tilde{z}$ and $\tilde{\psi}$ are differentiated as follows:

$$\begin{aligned} \dot{\tilde{z}} &= \dot{x}_d\cos(\psi_R) + \dot{y}_d\sin(\psi_R) - u\cos(\tilde{\psi}) - v\sin(\tilde{\psi}) \\ \dot{\tilde{\psi}} &= \dot{\psi}_R - r. \end{aligned} \tag{21}$$

Define intermediate control variables α_u and α_r to govern the u and r dynamics in the cascaded control structure:

$$\begin{aligned} \alpha_u &= \frac{\dot{x}_d\cos(\psi_R) + \dot{y}_d\cos(\psi_R) - v\sin(\tilde{\psi}) + k_{\tilde{x}}(\tilde{x} - \zeta_{xy})}{\cos(\tilde{\psi})} \\ \alpha_r &= k_{\tilde{\psi}}\tilde{\psi} + \dot{\psi}_R \end{aligned} \tag{22}$$

where $k_{\tilde{z}}$ and $k_{\tilde{\psi}}$ denote positive control gains.

By introducing a fresh state variable $\dot{\beta}_u$ and $\dot{\beta}_r$, duplicate differentiation of virtual controllers is avoided. First-order filtering of α_u and α_r with time constants t_u and t_r, $\dot{\beta}_u$ and $\dot{\beta}_r$ are given by the following:

$$\begin{aligned} t_i\dot{\beta}_i + \beta_i &= \alpha_i \\ \beta_{i_0} &= \alpha_{i_0}, i = u, r. \end{aligned} \tag{23}$$

Define the dynamic surface control tracking errors as follows:

$$\begin{aligned} y_i &= \alpha_i - \beta_i \\ \dot{\beta}_i &= \frac{y_i}{t_i}. \end{aligned} \tag{24}$$

Then, the derivatives of y_u, y_r can be obtained as follows:

$$\begin{aligned}\dot{y}_u =& \dot{\alpha}_u - \dot{\beta}_u \\ =& -\frac{y_u}{t_u} + \frac{\partial \alpha_u}{\partial \dot{x}_d}\ddot{x}_d + \frac{\partial \alpha_u}{\partial \dot{y}_d}\ddot{y}_d + \frac{\partial \alpha_u}{\partial \tilde{z}}\dot{\tilde{z}} + \frac{\partial \alpha_u}{\partial \psi_R}\dot{\psi}_R + \frac{\partial \alpha_u}{\partial \tilde{\psi}}\dot{\tilde{\psi}} \\ &+ \frac{\partial \alpha_u}{\partial v}\dot{v} \\ =& -\frac{y_u}{t_u} + B_u(\cdot) \\ \dot{y}_r =& \dot{\alpha}_r - \dot{\beta}_r \\ =& -\frac{y_r}{t_r} + \frac{\partial \alpha_r}{\partial \tilde{\psi}}\dot{\tilde{\psi}} + \frac{\partial \alpha_r}{\partial \psi_R}\ddot{\psi}_R \\ =& -\frac{y_r}{t_r} + B_r(\cdot)\end{aligned} \tag{25}$$

where $B_u(\cdot)$, $B_r(\cdot)$ are continuous functions.

For (22), the virtual control law α_u has no definition at $\tilde{\psi} = \pm 0.5\pi$, hence, in the control design, we first suppose that $|\tilde{\psi}| < 0.5$, and apply the following:

$$\tilde{\psi} = \begin{cases} \Theta - \pi, & \Theta \geq \frac{\pi}{2} \\ \Theta, & \frac{\pi}{2} < \Theta < \frac{\pi}{2} \\ \Theta + \pi, & \Theta \leq \frac{\pi}{2} \end{cases} \tag{26}$$

to ensure the assumption holds.

In (22), ζ_{xy} denotes a small positive constant. The term $(\tilde{z} - \zeta_{xy})$ incorporated into α_u ensures that the real ship generally tracks the virtual ship, aiding in satisfying the condition $|\tilde{\psi}| < 0.5\pi$ and ensuring the error variable $\tilde{z}$ converges to $\lim_{t\to\infty} \tilde{z} = \zeta_{xy}$. We select $\zeta_{xy} = exp(-0.054\tilde{z})$ in Section 5.

Step 2: Kinetic errors are characterized as $\tilde{u} = \beta_u - u$ and $\tilde{r} = \beta_r - r$, along with (6) and (24), we obtain the following:

$$\begin{aligned}\dot{\tilde{u}} &= \dot{\beta}_u - \frac{m_v}{m_u}vr + f_u - \frac{1}{m_u}[c\tau_u + d(\tau_u)] - d_{wu} \\ \dot{\tilde{r}} &= \dot{\beta}_r - \frac{(m_u - m_v)}{m_r}uv + f_r - \frac{1}{m_r}[c\tau_r + d(\tau_r)] - d_{wr}.\end{aligned} \tag{27}$$

The unknown dynamics f_i are approximated via neural network-based function approximators as per (28), with $i = u, r$:

$$\begin{aligned}F_u &= f_u - \frac{m_v}{m_u}vr \\ F_r &= f_r - \frac{(m_u - m_v)}{m_r}uv.\end{aligned} \tag{28}$$

Inferences are made using the following two important inequalities:

$$i_e^3 F_i \leq \frac{c^2}{2m_i^2} i_e^6 \lambda_i R_i(i) R_i(i)^\top + \frac{m_i^2}{2c^2} + \frac{3}{4}i_e^4 + \frac{1}{4}\varepsilon_i^4 \tag{29}$$

and

$$i_e^3 d(\tau_i) \leq \frac{3}{4}i_e^4 + \frac{1}{4}D^{*4}, i = u, r \tag{30}$$

The corresponding control law and parameter adjustment rules are defined as follows:

$$\begin{aligned}\tau_u &= \hat{\lambda}_u \Phi_u(\cdot)\tilde{u}^3 + k_{\tilde{u}}\tilde{u} + \dot{\beta}_u,\\ \tau_r &= \hat{\lambda}_r \Phi_r(\cdot)\tilde{r}^3 + k_{\tilde{r}}\tilde{r} + \dot{\beta}_r.\end{aligned} \tag{31}$$

and

$$\begin{aligned}\dot{\hat{\lambda}}_u &= \Gamma_u\left[\Phi_u(\cdot)\tilde{u}^6 - \zeta_u\left(\hat{\lambda}_u - \hat{\lambda}_{u0}\right)\right],\\ \dot{\hat{\lambda}}_r &= \Gamma_r\left[\Phi_r(\cdot)\tilde{r}^6 - \zeta_r\left(\hat{\lambda}_r - \hat{\lambda}_{r0}\right)\right].\end{aligned} \tag{32}$$

where $\Phi_u(\cdot) = c/2m_i R_i(i)R_i(i)^\top, i = u, r$ and $k_{\tilde{u}}, k_{\tilde{r}}, \zeta_u, \zeta_r, \Gamma_u, \Gamma_r$ are positive constant parameters. $\hat{\lambda}_i$ is the estimated value of λ_i, where $\hat{\lambda}_{i0}$ is the preliminary estimate of $\hat{\lambda}_i$.

4.2. Stability Analysis

Theorem 1. *Considering the underactuated vessel (1), (2), the virtual controls (22), the adaptive control scheme (31), and the MLP-guided adaptive law (32). All error signals in the underactuated vessel system can be driven to the performance region by adjusting control parameters appropriately, which are SGUUB.*

Proof. Define the Lyapunov candidate function V with the following energy-like structure (33):

$$\begin{aligned}V =& \frac{1}{4}\left(\tilde{z} - \zeta_{xy}\right)^4 + \frac{1}{4}\tilde{\psi}^4 + \frac{1}{4}y_u^4 + \frac{1}{4}y_r^4 + \frac{1}{4}\tilde{u}^4 + \frac{1}{4}\tilde{r}^4\\ &- \frac{c}{2m_u}\Gamma_u^{-1}\tilde{\lambda}_u^2 - \frac{c}{2m_r}\Gamma_r^{-1}\tilde{\lambda}_r^2.\end{aligned} \tag{33}$$

The derivation process for V yields the result in (34).

$$\begin{aligned}\dot{V} =& \left(\tilde{z} - \zeta_{xy}\right)^3\dot{\tilde{z}} + \tilde{\psi}^3\dot{\tilde{\psi}} + y_u^3\dot{y}_u + y_r^3\dot{y}_r + \tilde{u}^3\dot{\tilde{u}} + \tilde{r}^3\dot{\tilde{r}}\\ &- \frac{c}{m_u}\Gamma_u^{-1}\tilde{\lambda}_u\dot{\hat{\lambda}}_u - \frac{c}{m_r}\Gamma_r^{-1}\tilde{\lambda}_r\dot{\hat{\lambda}}_r.\end{aligned} \tag{34}$$

Combining with (21), (22), (26), (27) and Young's inequality, it is possible to obtain (35).

$$\begin{aligned}\left(\tilde{z} - \zeta_{xy}\right)^3\dot{\tilde{z}} + y_u^3\dot{y}_u \le& -k_{\tilde{z}}\left(\tilde{z} - \zeta_{xy}\right)^4 + \frac{3}{4}\left(\tilde{z} - \zeta_{xy}\right)^4 + \frac{1}{4}y_u^4\\ &+ \tilde{u}cos(\tilde{\psi})\left(\tilde{z} - \zeta_{xy}\right)^3 + \frac{B_u^2 y_u^2 M_u^2}{2bM_u^2}\\ &+ \frac{b}{2} - \frac{y_u^4}{t_u}\\ \le& -\left(k_{\tilde{z}} - \frac{3}{2}\right)\left(\tilde{z} - \zeta_{xy}\right)^4 + \frac{1}{4}y_u^4 + \frac{1}{4}\tilde{u}^4\\ &+ \frac{B_u^2 y_u^2 M_u^2}{2bM_u^2} + \frac{b}{2} - \frac{y_u^4}{t_u}.\end{aligned}$$

$$\begin{aligned}\tilde{\psi}^3\dot{\tilde{\psi}} + y_r^3\dot{y}_r \le& -k_{\tilde{\psi}}\tilde{\psi}^4 + \frac{3}{4}\tilde{\psi}^4 + \frac{1}{4}y_r^4 + \tilde{\psi}^3\tilde{r} + \frac{B_r^2 y_r^2 M_r^2}{2bM_r^2} + \frac{b}{2} - \frac{y_r^4}{t_r}\\ \le& -\left(k_{\tilde{\psi}} - \frac{3}{2}\right)\tilde{\psi}^4 + \frac{1}{4}y_r^4 + \frac{1}{4}\tilde{r}^4 + \frac{B_r^2 y_r^2 M_r^2}{2bM_r^2} + \frac{b}{2} - \frac{y_r^4}{t_r}.\end{aligned} \tag{35}$$

Substituting (27), (28) into (34) further gives (36).

$$\begin{aligned}\dot{V} \leq & -\left(k_{\tilde{z}}-\frac{2}{3}\right)(\tilde{z}-\zeta_{xy})^4-\left(k_{\tilde{\psi}}-\frac{2}{3}\right)\tilde{\psi}^4 \\ & -\sum_{i=u,r}\left(\frac{y_i^4}{t_i}-\frac{y_i^4}{4}-\frac{B_i^2y_i^2M_i^2}{2bM_i^2}-\frac{b}{2}\right)+\frac{1}{4}\tilde{u}^4+\frac{1}{4}\tilde{r}^4 \\ & +\tilde{u}^3\left\{\dot{\beta}_u+\theta_u+f_u(u)-\frac{1}{m_u}[c\tau_u+d(\tau_u)]\right\} \\ & +\tilde{r}^3\left\{\dot{\beta}_r+\theta_r+f_r(r)-\frac{1}{m_r}[\,c\tau_r+d(\tau_r)]\right\} \\ & -\frac{c}{m_u}\Gamma_u^{-1}\tilde{\lambda}_u\dot{\hat{\lambda}}_u-\frac{c}{m_r}\Gamma_r^{-1}\tilde{\lambda}_r\dot{\hat{\lambda}}_r.\end{aligned} \tag{36}$$

Using (29)–(32) and (36), we get (37):

$$\begin{aligned}\dot{V} \leq & -\left(k_{\tilde{z}}-\frac{2}{3}\right)(\tilde{z}-\zeta_{xy})^4-\left(k_{\tilde{\psi}}-\frac{2}{3}\right)\tilde{\psi}^4 \\ & -\sum_{i=u,r}\left(\frac{y_i^4}{t_i}-\frac{y_i^4}{4}-\frac{B_i^2y_i^2M_i^2}{2bM_i^2}-\frac{b}{2}\right)+\frac{1}{4}\tilde{u}^4+\frac{1}{4}\tilde{r}^4 \\ & -\sum_{i=u,r}\left(\frac{c}{m_i}\dot{\beta}_i i_e^3-\dot{\beta}_i i_e^3+i_e^3d_{wi}\right) \\ & +\sum_{i=u,r}\left[\frac{c}{m_i}\zeta_i\tilde{\lambda}_i(\hat{\lambda}_i-\hat{\lambda}_{i0})+\frac{m_i^2}{2c^2}+\frac{1}{4}e_i^4\right].\end{aligned} \tag{37}$$

According to Young's inequality we have the following:

$$\begin{aligned}\frac{c}{m_i}\dot{\beta}_i i_e^3-\dot{\beta}_i i_e^3 &\leq \frac{3}{4}i_e^4+\frac{1}{4}\left[\dot{\beta}_i\left(\frac{c}{m_i}-1\right)\right]^4 \\ &= \frac{3}{4}i_e^4+\frac{1}{4}\left(\frac{y_i}{t_i}\right)^4\left(\frac{c}{m_i}-1\right)^4 \\ i_e^3d_{wi} &\leq \frac{3}{4}i_e^4+\frac{1}{4}\bar{d}_{wi}^4 \\ \tilde{\lambda}_i(\hat{\lambda}_i-\hat{\lambda}_{i0}) &\leq \frac{1}{2}\tilde{\lambda}_i^2+\frac{1}{2}(\hat{\lambda}_i-\hat{\lambda}_{i0})^2.\end{aligned} \tag{38}$$

Substituting (38) into (37) gives (39):

$$\begin{aligned}\dot{V} \leq & -\left(k_{\tilde{z}}-\frac{2}{3}\right)(\tilde{z}-\zeta_{xy})^4-\left(k_{\tilde{\psi}}-\frac{2}{3}\right)\tilde{\psi}^4 \\ & -\sum_{i=u,r}\left(\frac{y_i^4}{t_i}-\frac{y_i^4}{4}-\frac{B_i^2y_i^2M_i^2}{2bM_i^2}-\frac{b}{2}\right)+\frac{1}{4}\tilde{u}^4+\frac{1}{4}\tilde{r}^4 \\ & -\sum_{i=u,r}\left[\frac{3}{2}i_e^4+\frac{1}{4}\left(\frac{y_i}{t_i}\right)^4\left(\frac{c}{m_i}-1\right)^4\right]+\frac{1}{4}\bar{d}_{wi}^4 \\ & +\sum_{i=u,r}\left\{\frac{c}{m_i}\zeta_i\left[\frac{1}{2}\tilde{\lambda}_i^2+\frac{1}{2}(\hat{\lambda}_i-\hat{\lambda}_{i0})^2\right]+\frac{m_i^2}{2c^2}+\frac{1}{4}e_i^4\right\}.\end{aligned} \tag{39}$$

Now that $k_{\tilde{z}}$, $k_{\tilde{\psi}}$ are all control design parameters. Now we can chose the following:

$$\begin{aligned} a_0 &= \min\left\{\frac{\zeta_u}{2\Gamma_u^{-1}}, \frac{\zeta_r}{2\Gamma_r^{-1}}\right\} \\ \frac{1}{t_i} &= \frac{M_i}{2b} + \frac{1}{4} + a_{0i} \\ k_{\tilde{z}} &= a_{\tilde{z}} + \frac{3}{4} \\ k_{\tilde{\psi}} &= a_{\tilde{\psi}} + \frac{3}{4} \end{aligned} \tag{40}$$

with a_{0i}, $a_{\tilde{z}}$, $a_{\tilde{\psi}}$ being positive constants.

Substituting (40) into (39) gives (41):

$$\begin{aligned} \dot{V} \leq & -\left(a_{\tilde{z}} - \frac{3}{4}\right)(\tilde{z} - \zeta_{xy})^4 - \left(a_{\tilde{\psi}} - \frac{3}{4}\right)\tilde{\psi}^4 \\ & - a_0 \sum_{i=u,r}\left(y_i^4 + i_e^4 + \frac{c}{m_i}\Gamma_i^{-1}\tilde{\lambda}_i^2\right) + \sigma \\ \leq & -2aV + \sigma \\ a = & \min\{a_{\tilde{z}} - \frac{3}{4}, a_{\tilde{\psi}} - \frac{3}{4}, a_0\} \\ \sigma = & b + \frac{1}{4}\bar{d}_{wi}^4 + \frac{1}{4}\left(\frac{c}{m_i} - 1\right)^4 + \frac{c}{2m_i}(\hat{\lambda}_i - \hat{\lambda}_{i0})^2 \\ & + \frac{m_i^2}{2c^2} + \frac{1}{4}e_i^4. \end{aligned} \tag{41}$$

The adaptive neural control design, which generates the key result of this paper, has now been finalized based on the backstepping method. □

5. Simulation

Numerical validation of the proposed controller's performance is demonstrated through the following simulation studies. To achieve this objective, we adopt the underactuated vessel dynamics model described in [40,41]. $m_u = 121 \times 10^3$, $m_v = 177.5 \times 10^3$, and $m_r = 637 \times 10^5$. The time-varying disturbances in the plant are as follows:

$$\begin{aligned} d_{wu} &= \frac{11}{12}(1 + 0.35\sin(0.2\mathrm{t}) + 0.15\cos(0.5\mathrm{t})) \\ d_{wv} &= \frac{26}{17.79}(1 + 0.2\sin(0.1\mathrm{t}) + 0.3\cos(0.4\mathrm{t})) \\ d_{wr} &= -\frac{950}{636}(1 + 0.1\sin(0.5\mathrm{t}) + 0.3\cos(0.3\mathrm{t})). \end{aligned} \tag{42}$$

The integration time step used in this simulation experiment is 0.01 s. The simulation was conducted in the MATLAB R2025b environment, employing the Euler method as the numerical solver. A virtual ship generates the reference path given by (6) and $u_d = 6.0$ m/s. Initial conditions follow the setup in (30), for controllers with parameter values in the range of (35). Both RBF NNs approximating f_u and f_r consist of 25 nodes, $l = 10$ with centers uniformly distributed in $[-5\ \mathrm{m/s}, 5\ \mathrm{m/s}]$ for f_u and $[-1\ \mathrm{rad/s}, 1\ \mathrm{rad/s}]$ for f_r and node widths set to $\eta_j = 5(j = 1, 2, \cdots, l)$.

5.1. Closed-Loop Performance Verification

Simulation outcomes are illustrated in Figure 5, which shows the entire phase, encompassing the turning process characterized by a 2000-m turning diameter. The heading angle is depicted in Figure 6. The corresponding position and heading variations are presented in Figure 7. Figure 8 presents the ship velocities in the surge, sway and yaw directions. Figure 9 presents the changes in control inputs. Figure 10 illustrates the temporal evolution of the adaptive parameter. The results are consistent with ship maneuvering practices.

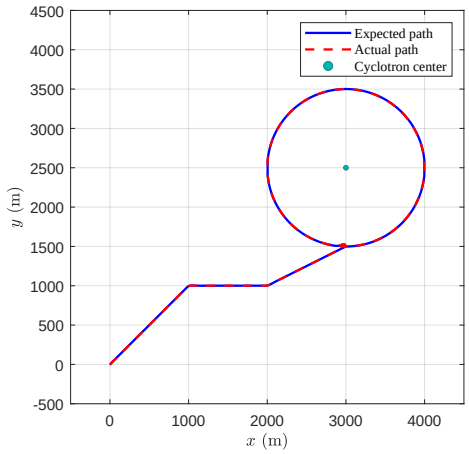


Figure 5. Trajectory of the underactuated vessel.

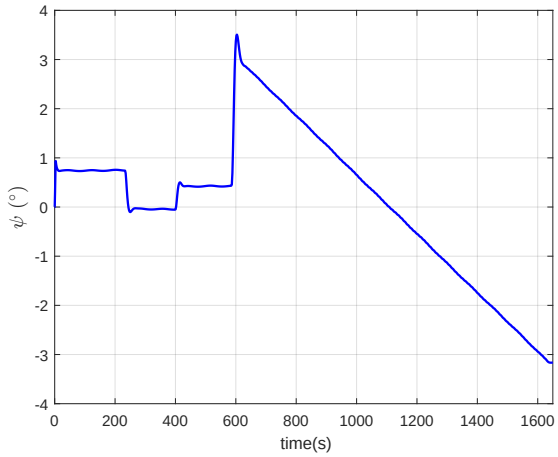


Figure 6. The yaw angle.

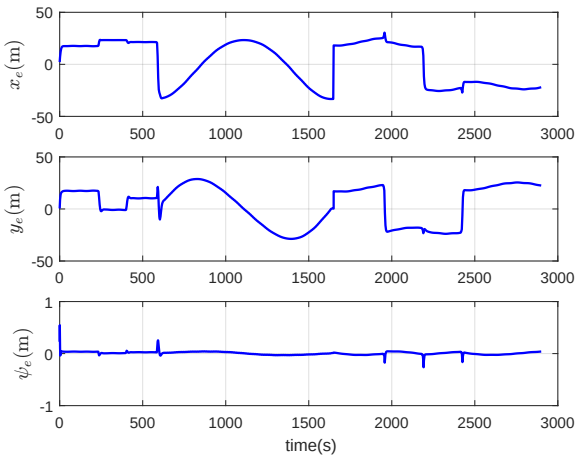


Figure 7. The path following error.

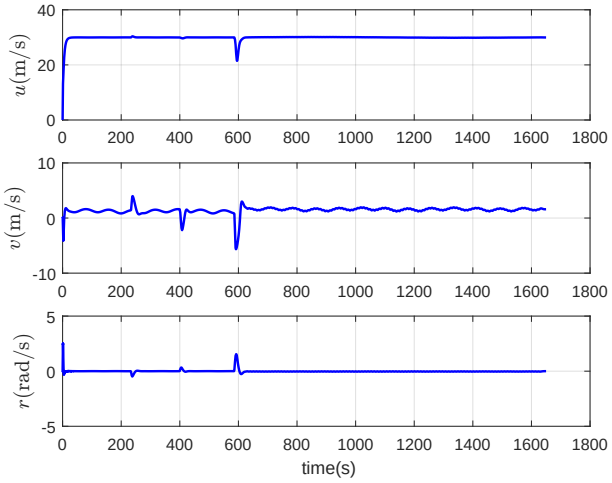


Figure 8. The velocity variables u, v, r.

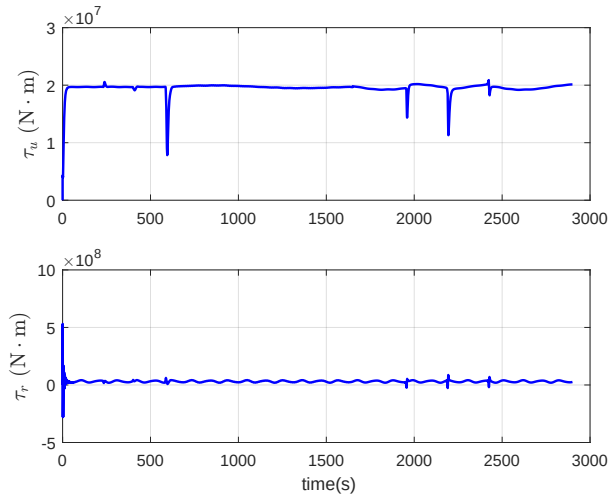


Figure 9. Control inputs.

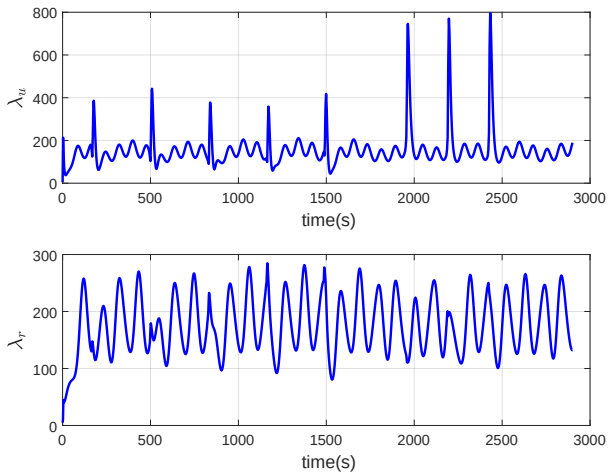


Figure 10. Adaptive time-varying parameter.

5.2. Comparison Simulation

First, this subpart verifies the effectiveness of the suggested adaptive neural path tracking control algorithm under hysteresis constraints. Second, its superiority in robustness

and control accuracy is demonstrated via simulations; a comparison is made between the proposed concise robust adaptive controller and the findings in [42].

$$\begin{aligned} &[x_{d_0}, y_{d_0}, \psi_{d_0}] = [0, 0, 0] \\ &[x_0, y_0, \psi_0, u_0, v_0, r_0] = [-70, 20, 0, 0, 0, 0] \end{aligned} \tag{43}$$

$$\begin{aligned} &\lambda_{u_0} = 5, \lambda_{r_0} = 5 \\ &k_{\tilde{z}} = 1.2, k_{\tilde{\psi}} = 5, k_{\tilde{u}} = 0.86 \times 10^6, k_{\tilde{r}} = 1.52 \times 10^9 \\ &\Gamma_u = 0.15, \Gamma_u = 2, \zeta_u = 0.25, \zeta_r = 1. \end{aligned} \tag{44}$$

Numerical simulations validate the effectiveness of the proposed approach, with comprehensive performance metrics illustrated in Figure 11. It displays the comparison of path following paths. In the simulation, complex reference paths are generated using waypoints $W_1(0\ \text{m}, 0\ \text{m})$, $W_2(0\ \text{m}, -1000\ \text{m})$, $W_3(2000\ \text{m}, -1000\ \text{m})$, $W_4(2000\ \text{m}, 1000\ \text{m})$, $W_5(0\ \text{m}, 1000\ \text{m})$, $W_6(0\ \text{m}, -1000\ \text{m})$, $W_7(2000\ \text{m}, 1000\ \text{m})$, $W_8(3000\ \text{m}, 0\ \text{m})$, $W_9(2000\ \text{m}, -1000\ \text{m})$, and $W_{10}(0\ \text{m}, 1000\ \text{m})$. It can be observed that with the proposed algorithm, the underactuated vessel is able to track the reference path from their initial position. Figure 12 shows the position and orientation error plots, with the red line showing the compared control schemes and the blue line showing the proposed algorithm. Comparative velocity profiles are demonstrated in Figure 13, highlighting the transient and steady-state behaviors differentials between the proposed and comparison methods. The control inputs for both control algorithms are given in Figure 14. Upon joint analysis, both control algorithms demonstrate satisfactory path-following performance, with the proposed algorithm displaying enhanced accuracy and stability. With respect to position and orientation errors, the proposed algorithm has a lower error value. In Figures 13 and 14, the proposed algorithm exhibits a much smaller error, and thus the algorithm has a high tracking accuracy and low energy consumption, with smooth energy change.

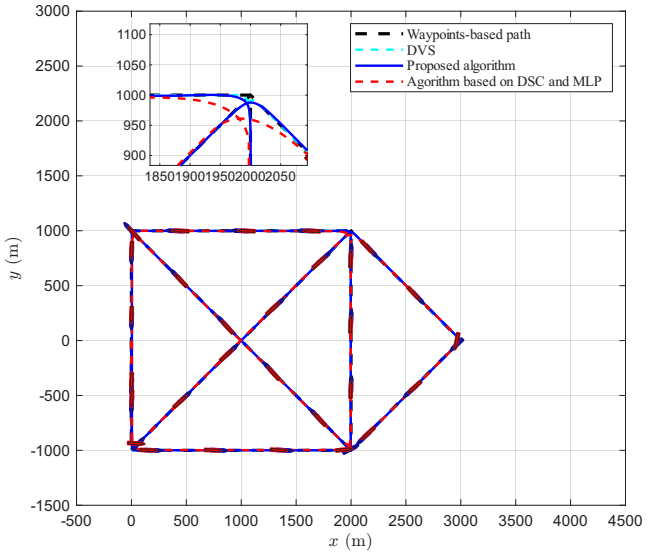


Figure 11. Plane trajectory diagram of ship path following.

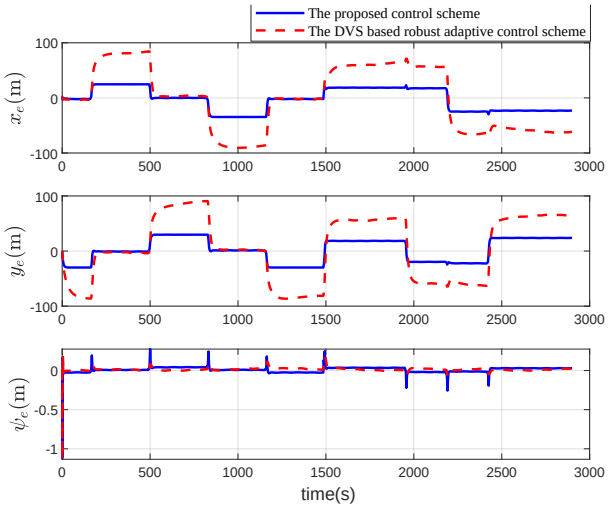


Figure 12. Position and heading angle errors of ships.

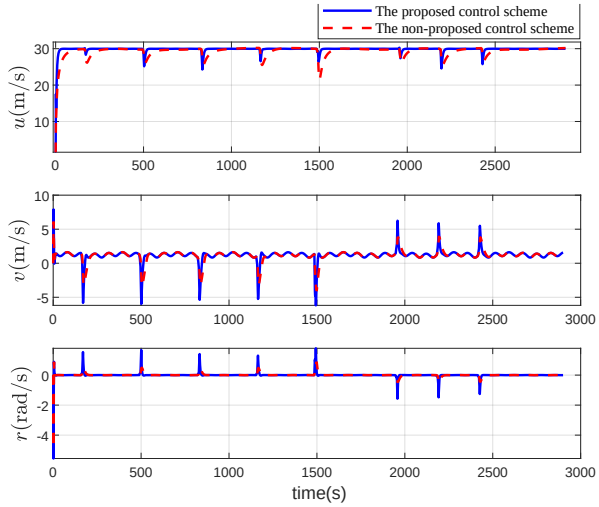


Figure 13. The velocity variables u, v, r.

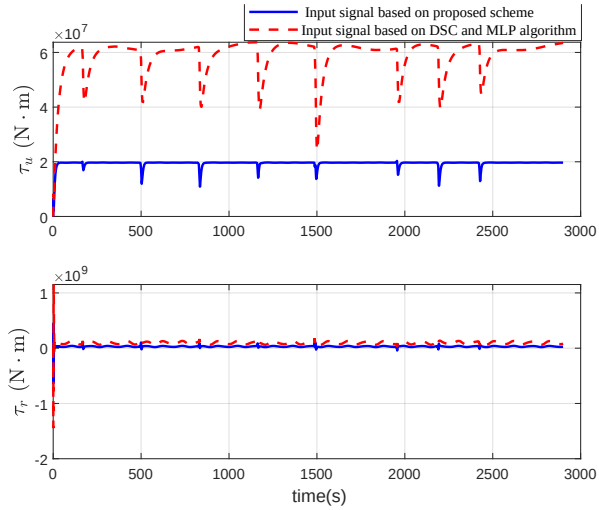


Figure 14. Control inputs of ships in surge and yaw DoFs.

To conduct a more in-depth quantitative analysis, three practical performance metrics (45) are introduced to evaluate the two algorithms: mean absolute error (MAE) reflects the system's stability capability, mean absolute control input (MAI) characterizes the

controller's energy consumption properties, and mean total input variation (MTV) describes the controller's smoothing performance.

$$\begin{aligned} \mathrm{MAE} &= \frac{1}{t_{\mathrm{end}} - 0} \int_0^{t_{\mathrm{end}}} |e(t)|\, dt, \\ \mathrm{MAI} &= \frac{1}{t_{\mathrm{end}} - 0} \int_0^{t_{\mathrm{end}}} |\tau(t)|\, dt, \\ \mathrm{MTV} &= \frac{1}{t_{\mathrm{end}} - 0} \int_0^{t_{\mathrm{end}}} |\tau(t+1) - \tau(t)|\, dt \end{aligned} \tag{45}$$

Detailed quantitative results are shown in Table 1. The MAE indicates that the vessel surge and sway position error of the proposed algorithm is significantly lower than that of the comparison approach in [42]. Although the value of the ψ_e term in our algorithm is higher than that in [42], the overall algorithm demonstrates comprehensive advantages in large-curved path following control. The MAI and MTV are evidently lower than the comparison algorithm, which indicates that the proposed algorithm is with lower control input and optimal controller structure.

Table 1. Quantitative outcomes for the proposed approach and the one in [42].

Indexes	Items	The Proposed Scheme	The Scheme in [42]
MAE	$x_{\mathrm{e}}(\mathrm{m})$	17.3266	48.2604
	$y_{\mathrm{e}}(\mathrm{m})$	18.7827	51.7442
	$\psi_{\mathrm{e}}(\mathrm{deg})$	1.5408	0.9544
MAI	$\tau_{\mathrm{u}}(\mathrm{N})$	1.9457×10^7	5.8827×10^7
	$\tau_{\mathrm{r}}(\mathrm{N} \cdot \mathrm{m})$	3.1123×10^7	9.7786×10^7
MTV	$\tau_{\mathrm{u}}(\mathrm{N})$	2334.2767	7732.6765
	$\tau_{\mathrm{r}}(\mathrm{N} \cdot \mathrm{m})$	1.3150×10^5	1.7026×10^5

6. Conclusions

In this paper, the path-following control of the underactuated vessel subject to environmental disturbance and backlash-like hysteresis nonlinearity is addressed. An improved L1-based guidance principle is introduced to eliminate the cumulative error of the yaw movement. Continuous dynamic correction of path-following errors fundamentally prevents the accumulation of yaw angle errors during prolonged vessel navigation. This effectively reduces overshoot during steering maneuvers, enabling smoother course adjustments and significantly enhancing tracking accuracy stability over long distances and complex paths. By fusion of the neural damping technique and quadratic function, the system's unknown dynamics and the backlash-like hysteresis nonlinearity are compensated simultaneously. Benefiting from the compressed NN weight adaptive mechanism, the structure of the proposed controller is optimized, which facilitates the implementation of the algorithm in practical engineering. Numerical simulation and quantitative comparison are conducted to verify the effectiveness and superiority of the proposed strategy. In the future, the performance of the control method in more severe marine environments should be studied further.

Author Contributions: Conceptualization, C.H. and B.Z.; methodology, C.H. and B.Z.; software, B.Z.; validation, C.H. and B.Z.; formal analysis, B.Z. and C.H.; investigation, B.Z.; resources, C.H. and H.X.; data curation, B.Z.; writing—original draft preparation, B.Z. and C.H.; writing—review and editing, C.H. and M.W.; visualization, C.H. and H.X.; supervision, C.H. and M.W.; project administration, C.H. and H.X.; funding acquisition, C.H. and M.W. All authors have read and agreed to the published version of the manuscript.

Funding: This work is partially supported by the National Natural Science Foundation of China (52501435), the Natural Science Foundation of Liaoning Province (2025-BS-0209), and the Fundamental Research Funds for the Central Universities (3132025135).

Institutional Review Board Statement: Not applicable.

Informed Consent Statement: Not applicable.

Data Availability Statement: The original contributions presented in this study are included in the article. Further inquiries can be directed at the corresponding author.

Acknowledgments: We extend our sincere gratitude to all contributors to this research. First, we thank the Intelligent Ship Control Laboratory at Dalian Maritime University and the relevant authors for their support. Additionally, we express our deep appreciation to the editorial team of JMSE and the anonymous reviewers for their insightful comments and constructive suggestions, which significantly enhanced the quality of this manuscript.

Conflicts of Interest: The authors declare no conflicts of interest.

References

1. Jiang, Z.-P. Controlling underactuated mechanical systems: A review and open problems. In *Advances in the Theory of Control, Signals and Systems with Physical Modeling*; Springer: Berlin/Heidelberg, Germany, 2010; pp. 77–88.
2. Zhang, G.; Sun, Z.; Li, J.; Huang, J.; Qiu, B. Iterative Learning Control for Path-Following of ASV with the Ice Floes Auto-Select Avoidance Mechanism. *IEEE Trans. Intell. Transp. Syst.* **2025**, *26*, 13927–13938. [CrossRef]
3. Zhang, G.; Li, Z.; Li, J.; Shu, Y.; Zhang, X. Reinforcement learning-driven autonomous navigation strategy for rotor-assisted vehicles via integral event-triggered mechanism. *Transp. Res. Part D Transp. Environ.* **2025**, *146*, 104841. [CrossRef]
4. Zhang, G.; Xing, Y.; Zhang, W.; Li, J. Prescribed Performance Control for USV-UAV via a Robust Bounded Compensating Technique. *IEEE Trans. Control Netw. Syst.* **2025**, *12*, 2289–2299. [CrossRef]
5. Wu, W.; Ji, R.; Zhang, W.; Zhang, Y. Transient-Reinforced Tunnel Coordinated Control of Underactuated Marine Surface Vehicles with Actuator Faults. *IEEE Trans. Intell. Transp. Syst.* **2024**, *25*, 1872–1881. [CrossRef]
6. Zhai, M.; Yang, T.; Wu, Q.; Guo, S.; Pang, R.; Sun, N. Extended Kalman Filtering-Based Nonlinear Model Predictive Control for Underactuated Systems with Multiple Constraints and Obstacle Avoidance. *IEEE Trans. Cybern.* **2025**, *55*, 369–382. [CrossRef]
7. Yang, N.; Chang, D.; Johnson-Roberson, M.; Sun, J. Energy-Optimal Control for Autonomous Underwater Vehicles Using Economic Model Predictive Control. *IEEE Trans. Control Syst. Technol.* **2022**, *30*, 2377–2390. [CrossRef]
8. Lee, S.-D.; Song, Y.-S.; Kim, D.-H.; Kang, M.-R. Path following Control of an Underactuated Catamaran for Recovery Maneuvers. *Sensors* **2022**, *22*, 2233. [CrossRef] [PubMed]
9. Zhai, M.; Sun, N.; Yang, T.; Fang, Y. Underactuated Mechanical Systems with Both Actuator and Actuated/Unactuated State Constraints: A Predictive Control-Based Approach. *IEEE/ASME Trans. Mechatron.* **2023**, *28*, 1359–1371. [CrossRef]
10. Wichlund, K.Y.; Sordalen, O.J.; Egeland, O. Control properties of underactuated vehicles. In *Proceedings of 1995 IEEE International Conference on Robotics and Automation*; IEEE: New York, NY, USA, 1995; Volume 2, pp. 2009–2014. [CrossRef]
11. Brockett, R.W. Differential geometric control theory. In *Differential Geometric Control Theory*; Birkhäuser Boston: Boston, MA, USA, 1983; pp. 49–135.
12. Bacciotti, A.; Rosier, L. Liapunov functions and stability in control theory. In *Liapunov Functions and Stability in Control Theory*; Springer: Berlin/Heidelberg, Germany, 2005; pp. 101–132.
13. Fossen, T.I. *Guidance and Control of Ocean Vehicles*; Butterworth-Heinemann: Oxford, UK, 1994; pp. 1–438.
14. Li, Z.; Li, R.; Bu, R. Path Following of Under-Actuated Ships Based on Model Predictive Control With State Observer. *J. Mar. Sci. Technol.* **2021**, *26*, 408–418. [CrossRef]
15. Du, B.; Yang, K.; Zhang, W.; Chen, H. Terminal Line-of-Sight Angle-Constrained Target Tracking Guidance for Unmanned Surface Vehicles. *IEEE Trans. Veh. Technol.* **2024**, *73*, 12515–12529. [CrossRef]
16. Zhang, G.; Zhang, X. A Novel DVS Guidance Principle and Robust Adaptive Path-Following Control for Underactuated Ships Using Low Frequency Gain-Learning. *ISA Trans.* **2015**, *56*, 75–85. [CrossRef]
17. Zhang, G.; Deng, Y.; Zhang, W.; Huang, C. Novel DVS Guidance and Path-Following Control for Underactuated Ships in Presence of Multiple Static and Moving Obstacles. *Ocean Eng.* **2018**, *170*, 100–110. [CrossRef]
18. Zhou, C.; Yuan, M.; Feng, C.; Ang, W.T. A Modified Prandtl–Ishlinskii Hysteresis Model for Modeling and Compensating Asymmetric Hysteresis of Piezo-Actuated Flexure-Based Systems. *Sensors* **2022**, *22*, 8763. [CrossRef]
19. Dai, Y.; Li, D.; Wang, D. Review on the Nonlinear Modeling of Hysteresis in Piezoelectric Ceramic Actuators. *Actuators* **2023**, *12*, 442. [CrossRef]

20. Al Janaideh, M.; Al Saaideh, M.; Tan, X. The Prandtl–Ishlinskii Hysteresis Model: Fundamentals of the Model and Its Inverse Compensator [Lecture Notes]. *IEEE Control Syst. Mag.* **2023**, *43*, 66–84. [CrossRef]
21. de la Morena, J.; Ramos, F.; Vázquez, A.S. Hysteresis Modeling of Soft Pneumatic Actuators: An Experimental Review. *Actuators* **2025**, *14*, 321. [CrossRef]
22. Ferradj, I.; Monteiro, E.; Roland, S.; Mechbal, N. Multiphysics Model and Hysteresis Compensation for Control of Electroactive Actuators. In *2025 IEEE/RSJ International Conference on Intelligent Robots and Systems (IROS)*; IEEE/RSJ Conference Committee, Ed.; IEEE Press: New York, NY, USA, 2025; pp. 3617–3622. [CrossRef]
23. Wang, Z.; Liu, G.; Qian, S.; Wang, D.; Wei, X.; Yu, X. Tracking Control With External Force Self-Sensing Ability Based on Position/Force Estimators and Non-Linear Hysteresis Compensation for a Backdrivable Cable-Pulley-Driven Surgical Robotic Manipulator. *Mech. Mach. Theory* **2023**, *183*, 105259. [CrossRef]
24. Lee, D.-G.; Baek, D.; Kim, H.; Kim, J.H.; Kwon, D.-S. Learning-Based Discrete Hysteresis Classifier Using Wire Tension and Compensator for Flexible Endoscopic Surgery Robots. *Int. J. Precis. Eng. Manuf.* **2023**, *24*, 83–94. [CrossRef]
25. Wang, W.; Zhang, J.; Xu, M.; Chen, G. Hysteresis Characteristics and MPI Compensation of Two-Dimensional Piezoelectric Positioning Stage. *Micromachines* **2022**, *13*, 321. [CrossRef]
26. Chen, Y.-Y.; Lan, Y.-J.; Zhang, Y.-Q. Robust Control Design Based on Perturbation Cancellation for Micro-Positioning Design with Hysteresis. *Actuators* **2021**, *10*, 278. [CrossRef]
27. Li, X.; Zhang, G.; Zhou, Y. Predefined-Time Adaptive Neural Network Decentralized Control for Large-Scale Interconnected Systems with Input Hysteresis. *ISA Trans.* **2025**, *158*, 363–373. [CrossRef]
28. Zhou, J.; Wen, C.; Zhang, Y. Adaptive Backstepping Control of a Class of Uncertain Nonlinear Systems with Unknown Backlash-Like Hysteresis. *IEEE Trans. Autom. Control* **2004**, *49*, 1751–1759. [CrossRef]
29. Wang, F.; Liu, Z.; Zhang, Y.; Chen, C.L.P. Adaptive Fuzzy Control for a Class of Stochastic Pure-Feedback Nonlinear Systems with Unknown Hysteresis. *IEEE Trans. Fuzzy Syst.* **2016**, *24*, 140–152. [CrossRef]
30. Ouyang, R.; Jayawardhana, B. Absolute Stability Analysis of Linear Systems with Duhem Hysteresis Operator. *Automatica* **2014**, *50*, 1860–1866. [CrossRef]
31. Zhang, G.; Yao, M.; Shan, Q.; Zhang, W. Observer-Based Asynchronous Self-Triggered Control for a Dynamic Positioning Ship with the Hysteresis Input. *Sci. China Inf. Sci.* **2022**, *65*, 212206. [CrossRef]
32. Wang, D.; Pei, H.; Yao, J.; Xu, W.; Kurths, J. Memory Feedback Signals in Nonlinear Coupled Pitch-Roll Ship Motions Under Narrow-Band Stochastic Excitations. *Mech. Syst. Signal Process.* **2023**, *192*, 110220. [CrossRef]
33. Perez, T.; Goodwin, G.C. Constrained Predictive Control of Ship Fin Stabilizers to Prevent Dynamic Stall. *Control Eng. Pract.* **2008**, *16*, 482–494. [CrossRef]
34. Ahmed, S.; Wang, H.; Tian, Y. Adaptive High-Order Terminal Sliding Mode Control Based on Time Delay Estimation for the Robotic Manipulators With Backlash Hysteresis. *IEEE Trans. Syst. Man Cybern. Syst.* **2021**, *51*, 1128–1137. [CrossRef]
35. Kong, L.; Lai, Q.; Ouyang, Y.; Li, Q.; Zhang, S. Neural Learning Control of a Robotic Manipulator with Finite-Time Convergence in the Presence of Unknown Backlash-Like Hysteresis. *IEEE Trans. Syst. Man Cybern. Syst.* **2022**, *52*, 1916–1927. [CrossRef]
36. Polycarpou, M.M.; Mears, M.J. Stable Adaptive Tracking of Uncertain Systems Using Nonlinearly Parametrized On-Line Approximators. *Int. J. Control* **1998**, *70*, 363–384. [CrossRef]
37. Wang, H.; Chen, B.; Liu, K.; Liu, X.; Lin, C. Adaptive Neural Tracking Control for a Class of Nonstrict-Feedback Stochastic Nonlinear Systems with Unknown Backlash-Like Hysteresis. *IEEE Trans. Neural Netw. Learn. Syst.* **2014**, *25*, 947–958. [CrossRef]
38. Xu, Y.; Zhang, G.Q.; Li, J.Q. Robust Adaptive Path-tracking Control for the USV-UAV System Using DSC and ELM. In *Proceedings of the 2024 43rd Chinese Control Conference (CCC)*; IEEE: New York, NY, USA, 2024; pp. 3161–3166. [CrossRef]
39. Li, T.; Li, R.; Wang, D. Adaptive Neural Control of Nonlinear MIMO Systems with Unknown Time Delays. *Neurocomputing* **2012**, *78*, 83–88. [CrossRef]
40. Li, J.H.; Lee, P.M.; Jun, B.H.; Lim, Y.K. Point-to-Point Navigation of Underactuated Ships. *Automatica* **2008**, *44*, 3201–3205. [CrossRef]
41. Do, K.D.; Pan, J. Global Robust Adaptive Path Following of Underactuated Ships. *Automatica* **2006**, *42*, 1713–1722. [CrossRef]
42. Zhang, G.; Zhang, X. Concise Robust Adaptive Path-Following Control of Underactuated Ships Using DSC and MLP. *IEEE J. Ocean. Eng.* **2014**, *39*, 685–694. [CrossRef]

Disclaimer/Publisher's Note: The statements, opinions and data contained in all publications are solely those of the individual author(s) and contributor(s) and not of MDPI and/or the editor(s). MDPI and/or the editor(s) disclaim responsibility for any injury to people or property resulting from any ideas, methods, instructions or products referred to in the content.